SAR Imaging and Interferometry Using Parameters Estimated from Raw Data

Dongliang Wang, Jun Yang, Guangcai Sun, Matthew Brolly, Xin Tao, Jianhua Xiao, Guoqing Sun, Youchuan Wan and Xiaoping Xin

Abstract

Due to the costs, sensitivity, and export policies of many governments, universities, and research institutions, particularly in developing countries, the ability to purchase, install and maintain high-accuracy inertial navigation system (INS) and global positioning system (GPS) is restricted. This paper presents a new method for SAR imaging and interferometry using parameters estimated from raw data. First, methods for determining the order of real and imaginary parts within the raw data images, and for determining chirp rate polarity are proposed. Second, a selection of parameters, including the forward effective velocities of the sensor, the near range distance, and the squint angle, are extracted using the Doppler centroid and Doppler rate. Finally, we create single look complex (SLC) images, coherence maps, digital elevation models (DEMs), and dual-pass differential unwrapped phase maps. The level of accuracy shown in this comparative study suggests that the proposed method is acceptable for creating the featured SAR products and is suitable for real world applications. This method and result is particularly relevant for systems which suffer from a lack of high-accuracy positional metadata.

Introduction

Satellite SAR platforms generally orbit at heights significantly above the Earth's atmosphere and record precise orbit data; for example, The ALOS/PALSAR system orbits at 697 km above the Earth's surface. At such altitudes the effects of short-period motion compensation and orbit errors are less significant than at lower orbits or airborne flight altitudes. When processing satellite SAR data in the azimuth direction, the Doppler centroid and the frequency rate may be calculated using accurate spacecraft ancillary data incorporating information including the near range distance and velocity. These satellite GPS-determined parameters may be directly employed for DEM generation (Rossi *et al.*, 2012; Martone *et al.*, 2012; Crosetto, 2002) and deformation monitoring (Dell'Acqua and Polli, 2011; Gerke and Kerle, 2011; Jones and Davis, 2011; Kaya *et al.*, 2011; Zhang *et al.*, 2012; Gernhardt and Bamler, 2012; Herrera, 2009). For airborne SAR platforms, the motion errors can be considerably higher than those associated with equivalent spaceborne platforms due to atmospheric turbulence and the associated aircraft properties such as the relatively small size of the craft. This makes the need for motion compensation (MOCO) in airborne SAR operations more pressing than required when using higher altitude SAR systems (Xing *et al.*, 2009).

Due to the costs, sensitivity, and export policies, many universities or institutes in developing countries, including China, are unable to buy and install the high-accuracy INS and GPS systems on airborne SAR platforms required for high accuracy orbit calculations (Cumming and Li, 2007; Kong *et al.*, 2005; Wu *et al.*, 2013; Cao *et al.*, 2010). Therefore, more accurate information regarding the near range distance and forward velocities must be obtained using alternative methods to the typical methods employed to estimate values from the received radar data (Madsen, 1989; Jin, 1986; Bamler, 1991; Yu and Zhu, 1997; Wong and Cumming, 1996; Bamler and Runge, 1991; Cumming and Li, 2007; Kong *et al.*, 2005; Calloway and Donohoe, 1994; Samczynski and Kulpa, 2010; Wahl *et al.*, 1994; Berizzi *et al.*, 2002; Dall, 1991; Wu *et al.*, 2013; Cao *et al.*, 2010). In general it is a difficult undertaking to ascertain and verify the accuracy of the estimated near range distance and velocities recorded in airborne SAR systems in the absence of high-precision flight data.

In this study, we analyze the accuracy of the near range distance, velocities, accelerations, and displacement rates in the line of sight (LOS) direction calculated using data estimated from a raw data pair of ALOS/PALSAR scenes. The data are accompanied by high-precision orbit data contained within the recorded meta data files and serve as a direct comparison to establish the accuracy exhibited by the novel methods introduced in this work.

Dongliang Wang is with the National Hulunber Grassland Ecosystem Observation and Research Station, Institute of Agricultural Resources and Regional Planning, Chinese Academy of Agricultural Sciences, Beijing 10081, China and the School of Remote Sensing and Information Engineering, Wuhan University, Wuhan 430079, China (WDLGIS@gmail.com).

Jun Yang and Guangcai Sun are with the National Key Laboratory of Radar Signal Processing, Xidian University, Xi'an 710071, China.

Matthew Brolly is with the School of Environment and Technology, University of Brighton, Brighton BN2 4GJ, UK.

Xin Tao and Guoqing Sun are with the Department of Geographical Sciences, University of Maryland, College Park, MD 20742.

Jianhua Xiao is with the Wuhan Geomatics Institute, and the Key Laboratory of Precise Engineering & Industry Surveying of National Administration of Surveying, Mapping & Geoinformaton, Wuhan 430022, China.

Youchuan Wan is with the School of Remote Sensing and Information Engineering, Wuhan University, Wuhan 430079, China.

Xiaoping Xin is with the National Hulunber Grassland Ecosystem Observation and Research Station, Institute of Agricultural Resources and Regional Planning, Chinese Academy of Agricultural Sciences, Beijing 10081, China

Photogrammetric Engineering & Remote Sensing
Vol. 80, No. 5, July 2014, pp. 663–674.
0099-1112/14/8007–663

doi: 10.14358/PERS.80.7.663

The ALOS system was launched by the Japanese Aerospace Exploration Agency (JAXA) on the 24 January 2006. PALSAR features a high-precision inertial navigation system (INS) and global positioning system (GPS), and is designed with two advanced technologies. First, it possesses high speed and large capacity mission data handling technology and second, it benefits from precision spacecraft position and attitude determination capabilities. It is shown in Nakamura (Nakamura *et al.*, 2007) that the GPS-determined orbits are consistently located within −30 cm ±30 cm of the absolute evaluation determined by Satellite Laser Ranging (SLR) data, and as a result may be considered extremely accurate.

In this study we work under the assumption that the following parameters of SAR data are uncertain and need to be determined or estimated with greater accuracy:

1. The order of real and imaginary parts of raw data. These may be normal or inverted with the real part stored either before or after the imaginary part, respectively. The sign of the chirp rate may be positive or negative. This implies that the pulses generated in the SAR system may be "down-chirped" pulses (frequency decreases over time) or "up-chirped" pulses (frequency increases over time).
2. Additionally, we work under the assumption that for whatever reason, the accurate orbit data may be prohibitive for direct use and as a consequence, the forward velocities, the forward accelerations, and displacement rate in the LOS direction are only obtainable from raw data focusing.

The purpose of this study is then to analyze the use of parameters calculated from accurate orbit metadata in comparison to those found using the raw data parameter estimation methods presented in this study. This study will determine whether the values produced using the novel method are sufficiently accurate for raw data focusing and subsequent interferometry as determined through comparison with the standard methods. We will first use our proposed methods to estimate the chosen parameters for a pair of ALOS/PALSAR raw data scenes, and compare those estimated parameters with those calculated using the standard orbit data. We will also compare the DEMs and dual-pass differential unwrapped phase maps created using the standard accurate orbit data parameters and those created using estimated parameters.

This paper is organized as follows. First, the study data consisting of the pair of Level 1.0 ALOS/PALSAR raw data scenes are introduced; second, the methods for parameter estimation used for focusing raw data are described. These include the determination of the order of real and imaginary parts of raw data geometrically and mathematically, the determination of the sign of chirp rate in range, the estimation of the Doppler centroid and Doppler rate, and the estimation of the effective velocities of the sensor, the near range distance, and squint angle at the reference range. Additionally the forward accelerations and displacement rate in LOS direction are estimated. Third, the description of an experiment and subsequent analysis of the accuracy of SLCs, DEMs and dual-pass differential unwrapped phase maps created using these estimated parameters is provided. Finally, the conclusions are presented.

Study Data

The data used in this study include two scenes of ALOS/PALSAR HV-polarized raw data captured on 14 July 2007, and 29 August 2007, respectively (46 day repeat time). The data size is 5,152(in range) × 35,421(in azimuth). The primary study site is located in the town of Lushuihe, Jielin Province, China. The first scene is referred to as "070714," and the second as "070826". Table 1 summarizes the parameters used in this study and corresponding to the chosen scenes.

Methods

In this section, the methods for parameter estimation, required for raw data focusing are introduced. First, we propose a method for determination of the order of real and imaginary

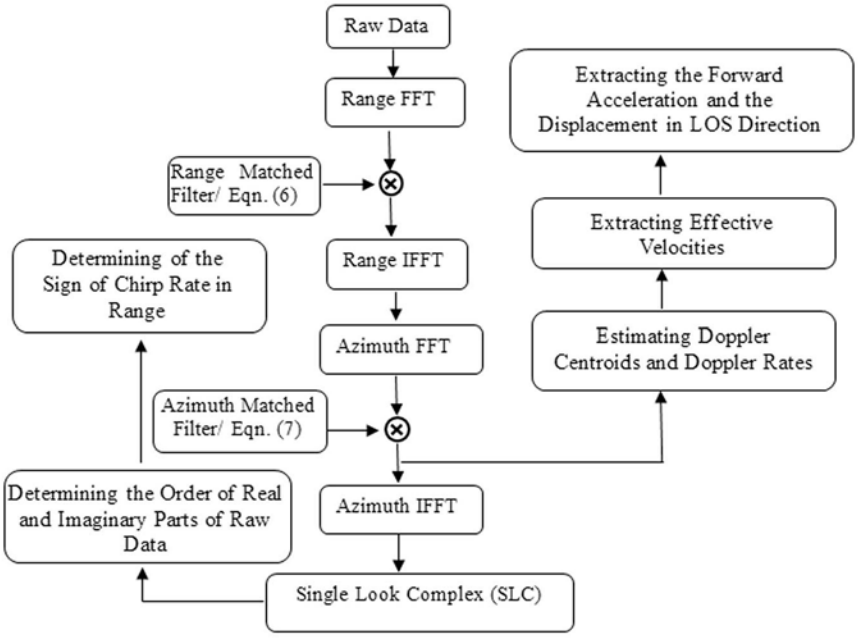

Figure 1. Flowchart for estimation of Parameters for Raw Data Focusing. The order of real and imaginary parts of raw data is determined after azimuth inverse fast Fourier transform (IFFT) and before determination of the sign of chirp rate in range. The forward effective velocities, the forward acceleration and the displacement in LOS direction are extracted based on the Doppler centroids and Doppler rates that are estimated from the data after azimuth fast Fourier transform (FFT) transformation.

Table 1. Parameters of Two Scenes of ALOS/PALSAR Level 1.0 Raw Data

Parameter Name	Value (Scene = 070714)	Value (Scene = 070826)
Near-Range Distance	848,815 m	848,665 m
Range Sampling Rate	16000000 s^{-1}	16000000 s^{-1}
Carrier Wave Frequency	1.27 x109 Hz	1.27 x109 Hz
Chirp Rate	(–)5.18519 ×1011Hz·s^{-1}	(–)5.18519 ×1011 Hz·s^{-1}
Antenna Length	8.9 m	8.9 m
Platform Velocity	~7,592 m·s^{-1}	~7,593 m·s^{-1}
Pulse Repetition Frequency	2159.827 Hz	2159.827 Hz
Doppler Rate	'540.70 Hz·s^{-1}	'511.61 Hz·s^{-1}
Squint Angle	~0.162°	~0.095°

parts of raw data. Subsequently, we propose a method for determination of the sign of the chirp rate. Finally, the Doppler centroids and Doppler rates are estimated using the "minimum entropy via subspace autofocus (MESA)" method (Cao *et al.*, 2010). This is followed by estimation of the effective velocities of the sensor, the near range distance, the squint angle, and the estimation of the forward acceleration and displacement rate in LOS direction. Figure 1 shows the flowchart for parameter estimation.

Determination of the Order of Real and Imaginary Parts of Raw Data

A simple geometrical description of a side-looking SAR imaging system is shown in Figure 2. The platform moves along the x-axis in the azimuth direction with velocity v. P(R_B,X) is an illuminated point on the ground. R_B represents the distance of closest approach with respect to the x-axis. X represents the x coordinate of the illuminated point. R_o is the distance from P to the sensor. vt_m represents the x coordinate of the sensor position at azimuth time t_m.

Assume that the radar emits chirp pulses, and the echo signal received from a point target can be expressed by (Zhang *et al.*, 2013):

$$s\left(\hat{t},t_m\right)=w_r\left(\hat{t}-\frac{2R\left(t_m\right)}{c}\right)w_a\left(t_m\right)\exp\left(-j\pi k_r\left(\hat{t}-\frac{2R\left(t_m\right)}{c}\right)^2\right)\exp\left(-j\frac{4\pi}{\lambda}R\left(t_m\right)\right) \quad (1)$$

where $\hat{t}$ is the fast time; c is the light speed; $W_r(\cdot)$ and $W_a(\cdot)$ represent the range and azimuth envelopes, respectively; λ is the wavelength; k_r is the chirp rate; $R\left(t_m\right)=\sqrt{R_B^2+(X-vt_m)^2}$, where, as stated above, R_B is the range from the Doppler centroid point to sensor; t_m is the azimuth time, vt_m is the x coordinate of the sensor position, and X is the x coordinate of the illuminated point target. When the squint angle of radar antenna radiation is 0° (the Doppler centroid is zero), the range distance of $R(t_m)$ can be written as $R(t_m)=\frac{\left(vt_m\right)^2}{2R_B}$ and Equation 1 then becomes:

$$s(t,t_m)=w_r\left(t-\frac{2R\left(t_m\right)}{c}\right)w_a(t_m)\,exp(-j\pi k_r\left(\hat{t}-\frac{2R\left(t_m\right)}{c}\right)^2)exp(-j\frac{4\pi}{\lambda}R_B)exp(-j\frac{4\pi}{\lambda}k_aR_Bt_m^2) \quad (2)$$

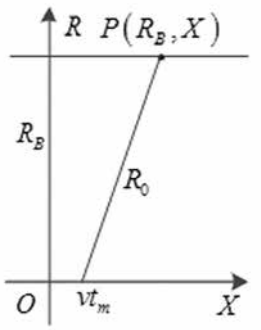

Figure 2. Geometry of side-looking-mode SAR imaging

where

$$k_a=-\frac{2v^2\cos^2(\beta)}{\lambda R_B}. \quad (3)$$

In these equations β represents the squint angle of the LOS with respect to the line perpendicular to the nominal trajectory and k_a the azimuth Doppler rate. Following the application of a range Fourier transform, the echo signal in the range-Doppler domain can be presented as:

$$S\left(f_r,t_m\right)=W_r\left(f_r\right)w_a\left(t_m\right)\exp\left(-j\pi\frac{f_r^2}{k_r}\right)\exp\left(-j\frac{4\pi}{\lambda}R_B\right)\exp\left(j\pi k_at_m^2\right) \quad (4)$$

where f_r is the range frequency. Similarly, after applying the azimuth Fourier transform, the echo signal in the range-azimuth frequency domain may be expressed as:

$$S\left(f_r,f_a\right)=W_r\left(f_r\right)w_a\left(f_a\right)\exp\left(-j\pi\frac{f_r^2}{k_r}\right)\exp\left(-j\frac{4\pi}{\lambda}R_B\right)\exp\left(j\pi\frac{f_a^2}{k_a}\right) \quad (5)$$

where f_a is azimuth frequency. Thus, we can employ the following matched filters in order to adequately focus the raw data:

$$sref_r\left(\hat{t}\right)=\exp\left(-j\pi k_r\hat{t}^2\right) \quad (6)$$

$$sref_a(t_m;R_B)=a_r(t_m)\exp(-j\pi k_at_m^2) \quad (7)$$

where Equations 6 and 7 are the range and azimuth matched filters, respectively. Now, suppose the signal represented in Equation 1 can be written as a complex number:

$$s\left(\hat{t},t_m\right)=a+jb \quad (8)$$

with the phase of $s(\hat{t},t_m)$ given as $\phi(.) = atan(b/a)$. If the real and imaginary parts are then inverted, the signal from a point target may be written as a new complex number:

$$s'\left(\hat{t},t_m\right)=a+jb \quad (9)$$

The phase of $s'(\hat{t},t_m)$ is then $\phi'(.) = atan(b/a) = \pi/2 - \phi(.)$. Thus:

$$s'\left(\hat{t},t_m\right)=s^*\left(\hat{t},t_m\right)\exp\left(-j\frac{\pi}{2}\right) \quad (10)$$

where * is the complex conjugate notation. Equation 10 can

then be rewritten as shown in Equations 11 and 12 following the application of range and azimuth Fourier transforms, respectively:

$$S'(f_r', t_m) = FFT_i\left(s^*(t', t_m)\exp\left(-j\frac{\pi}{2}\right)\right) = S^*(-f_r, t_m) * \exp\left(-j\frac{\pi}{2}\right) \quad (11)$$

$$\begin{aligned} S'(f_r', f_a') &= FFT_{i_m}\left(S^*(-f_r, t_m) * \exp\left(-j\frac{\pi}{2}\right)\right) \\ &= S^*(-f_r, -f_a) * \exp\left(-j\frac{\pi}{2}\right) \\ &= W_r(-f_r) W_a(-f_a) \exp\left(-j\pi\frac{f_r^2}{-k_r}\right) \exp\left(-j\frac{4\pi}{\lambda}R_B\right) \exp\left(j\pi\frac{f_a^2}{-k_a}\right) * \exp\left(-j\frac{\pi}{2}\right) \end{aligned} \quad (12)$$

If we now compare Equations 5 and 12, we can deduct that the chirp rate of the new complex number can be defined as:

$$k_r' = -k_r \quad (13)$$

and the Doppler rate of the new complex number is:

$$\frac{2v^2 \cdot \cos^2(\beta)}{\lambda R_B} \quad (14)$$

We can further simplify this expression as when the squint angle β is very small, such as in this study, the Doppler rate approximately reduces to:

$$k_a' = -k_a \approx \frac{2v^2}{\lambda R_B}. \quad (15)$$

Contrary to the typical processing algorithms we require an image sourced from opposite matched filters both in range and azimuth as shown by Equations 16 and 17.

$$sref_r(\hat{t}) = \exp -j\pi(-k_r)\hat{t}^2) \quad (16)$$

$$sref_a(t_m; R_B) = a_r(t_m)\exp(-j\pi(-k_a)\hat{t}_m^2) \quad (17)$$

The generated chirp in the SAR system can display signal characteristics of frequency increases ("up-chirp") or decreases ("down-chirp") as a function of time, thus it is hard to directly determine the sign of chirp rate. However, the Doppler rate should always be negative, as shown in Equation 3. As a consequence, the following criterion may be employed to determine the order of real and imaginary parts of raw data:

1. By obtaining a correctly focused image using Equations 7 and 6, or using Equations 7 and 16, the order of real and imaginary parts is normal. Hence, the real part is stored before the imaginary.
2. By obtaining a correctly focused image using Equations 17 and 6, or using Equations 17 and 16, the order of the real and imaginary parts is inverted. Hence, the real part is stored after the imaginary part.

   For example, the four permutations of chirp rates (Hz·s^{-1}) and Doppler rates (Hz·s^{-1}), $(5.18519 \times 10^{11}, \frac{2v^2}{\lambda R_B})$, $(-5.18519 \times 10^{11}, \frac{2v^2}{\lambda R_B})$, $(5.18519 \times 10^{11}, \frac{2v^2}{\lambda R_B})$, and $(-5.18519 \times 10^{11}, \frac{2v^2}{\lambda R_B})$, were used to define the range and azimuth matched filters, respectively. The focused results are shown in Figure 3a through 3d.

In Figure 3, the only correctly focused image is the one shown in (3d). In this image, the chirp rate –5.18519 x10^{11} Hz·s^{-1} and Doppler rate $-2v^2/(\lambda R_B)$ (Hz·s^{-1}) were employed to define range and azimuth matched filters, respectively. According to the above criterion for determining the order of real and imaginary parts, we can draw conclusions that the real and imaginary parts are normal, specifically that the real part is stored in order before the imaginary part.

If the positions of the real and imaginary parts of raw data were artificially exchanged, the results focused using the same range and azimuth matched filters as used for Figure 3a through 3d will produce images as shown in Figure 4a through 4d. In Figure 4, the image depicted in (4a) is the only one to be correctly focused, this is for the scenario where a chirp rate of 5.18519 x10^{11} Hz·s^{-1} and Doppler rate of $2v^2/(\lambda R_B)$ (Hz·s^{-1}) (Hz·s^{-1}) were employed to define the range and azimuth matched filters, respectively. The above criterion is again successful in determining the order of real and imaginary parts.

Note that, the initial velocities listed in Table 1 are approximately 300 m·s^{-1} away from the accurate effective velocities, representing a 6 percent difference, but are able to be employed for obtaining discernible SLC data, as shown in Figures 3 and 4. The accurate effective velocities values will be estimated later.

Determination of the Sign of Chirp Rate in Range

After analysis of the raw data and determining the order of real and imaginary parts, the sign of chirp rate in the range direction may then be determined from the correctly focused SLC images. In Figure 3, the real and imaginary parts of the raw data are in the correct order, with (3d) being the only image correctly focused, corresponding to a chirp rate of –518519 ×10^6 Hz·s^{-1} and Doppler rate of $-2v^2/(\lambda R_B)$ (Hz·s^{-1}) (Hz·s^{-1}). Therefore, the chirp rate of the raw data must be –5.18519 ×10^{11} Hz·s^{-1}. The pulses generated in the ALOS/PALSAR system are therefore "down-chirped" pulses showing a frequency decrease with time.

Estimation of the Doppler Centroid and Doppler Rate

In SAR signal processing, high azimuth resolution may be obtained by coherently processing the Doppler histories of the return signal. This procedure is called azimuth compression, in which several important parameters such as the Doppler centroid and Doppler frequency rate are required (Cao *et al.*, 2010). These may be estimated from raw data. Estimation of Doppler centroid and Doppler frequency rate are traditionally called clutter-lock and autofocus, respectively.

In SAR systems, the azimuth data are acquired in a sampled fashion, with the sampling rate given by the pulse repetition frequency (PRF). Because of the spectral repetition of the sampled data, the Doppler centroid estimate is usually observed in two parts: the baseband Doppler centroid (expressed as a fraction of the PRF) and the Doppler ambiguity (expressed as an integer multiple of the PRF). Several clutter-lock techniques have been proposed so far. Some examples are energy balancing (ΔE), correlation Doppler estimator (CDE), sign Doppler estimator (SDE) (Madsen, 1989), and maximum-likelihood estimation (MLE) (Jin, 1986).The performances of these algorithms are compared in BaMLEr, (1991) and Yu and Zhu, (1997). These form the baseband algorithms that were incapable of resolving Doppler ambiguity and do not work well if partially exposed strong targets exist in the raw data. Such raw data can be obtained from scenes which feature high-contrast such as urban and coastal areas. To resolve the Doppler ambiguity, some Doppler ambiguity resolvers (DARs) are proposed, such as multi-look cross-correlation (MLCC) and multi-look beat frequency (MLBF) (Wong and Cumming,1996), the range look correlation technique (Cumming, 1986), and the wavelength diversity algorithm (WDA) (BaMLEr and Runge, 1991). The range looking correlation technique estimates the Doppler

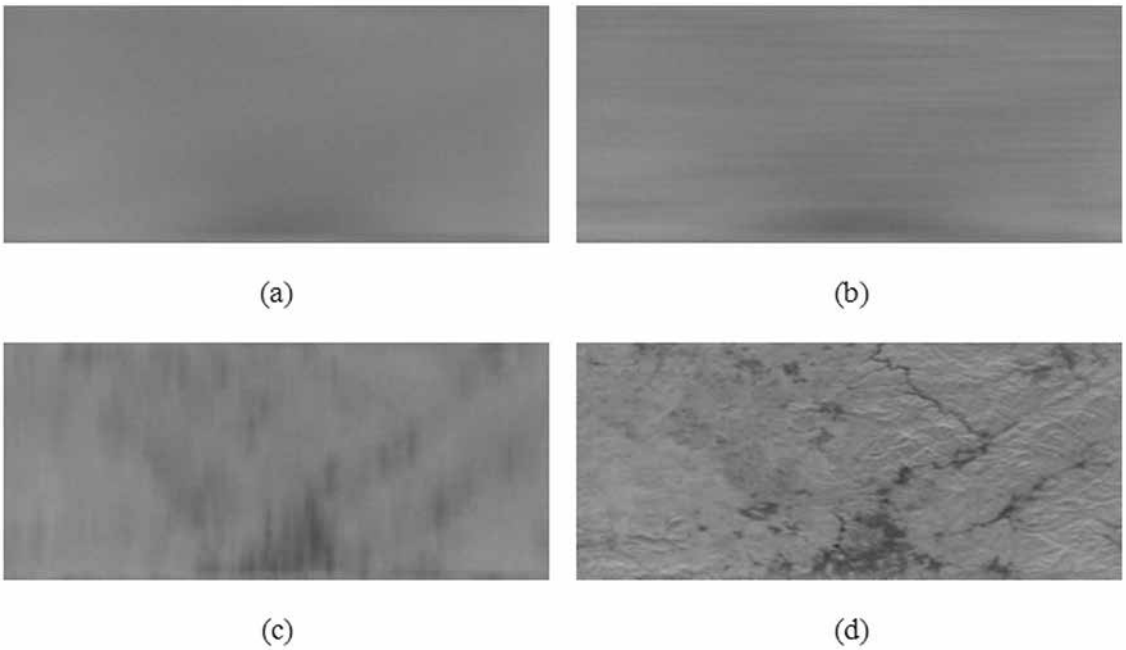

Figure 3. The focused results of the original raw data using four possible permutations of chirp rates ($Hz \cdot s^{-1}$) and Doppler rates ($Hz \cdot s^{-1}$): (a) (5.18519 x10^{11}, $\frac{2v^2}{\lambda R_B}$), (b) (-5.18519 x10^{11}, $\frac{2v^2}{\lambda R_B}$), (c) (5.18519 x10^{11}, $-\frac{2v^2}{\lambda R_B}$), and (d) (-5.18519 x$10^{11}$, $-\frac{2v^2}{\lambda R_B}$).

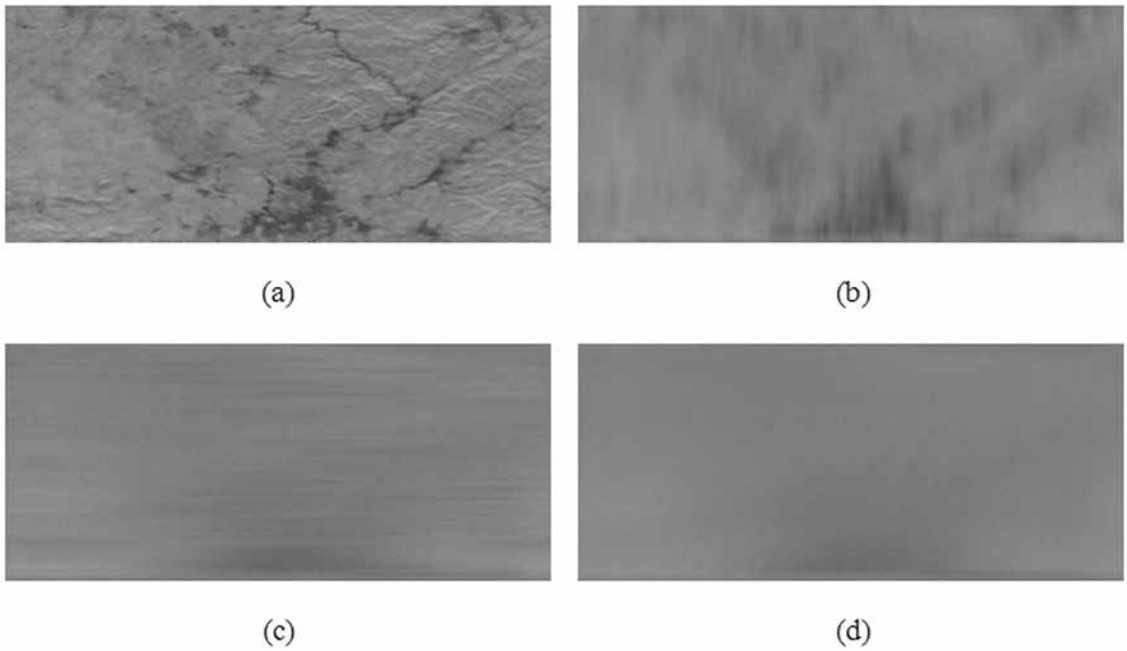

Figure 4. The focused results of the original raw data using four possible permutations of chirp rates ($Hz \cdot s^{-1}$) and Doppler rates ($Hz \cdot s^{-1}$): (a) (5.18519 x10^{11}, $\frac{2v^2}{\lambda R_B}$), (b) (-5.18519 x10^{11}, $\frac{2v^2}{\lambda R_B}$), (c) (5.18519 x10^{11}, $-\frac{2v^2}{\lambda R_B}$), and (d) (-5.18519 x$10^{11}$, $-\frac{2v^2}{\lambda R_B}$).

ambiguity only, and as this lacks sensitivity, its reliability is not guaranteed for all cases. WDA and MLCC-MLBF can estimate the Doppler centroid and can resolve the Doppler ambiguity, which was further improved by (Cumming and Li, 2007). WDA works best in the low-contrast scenes. MLCC-MLBF seems to be the best algorithm so far that estimates both the Doppler centroid and the Doppler ambiguity. However, its computational load is somewhat high, as it requires fast Fourier and inverse fast Fourier transforms to generate multi-looked range-compressed data. Kong *et al.* (2005) proposed an ambiguity-free algorithm to estimate both the Doppler centroid and the Doppler ambiguity number. The method utilizes the range walk response of targets induced by the squinted beam and does not use the signal power spectra. The ambiguity problem is hence not introduced. It requires no Fourier transform and is performed in a down-sampled range-compressed domain.

The Doppler centroid f_{dc} may be expressed as:

$$f_{dc} = \frac{2v * \sin\beta}{\lambda} \quad (18)$$

According to Equation 18, the Doppler centroid f_{dc} at the reference range is ~180 Hz, while the Doppler bandwidth *Ba* is ~1653.9 Hz with *PRF* of 2159.827 Hz, thus there is no Doppler ambiguity, and we only require estimates of the baseband Doppler centroid. The sign Doppler estimator (SDE) (Madsen, 1989) is very simple to implement within the processing of SAR data, particularly ALOS/PALSAR, so it was employed to estimate the Doppler centroid. The estimated Doppler centroids of "070714" are shown in Figure 5, varying as a function of range from 85 to 121 Hz. The Doppler centroid at the reference range is 102.95 Hz.

The Doppler rate is another factor that can affect the quality of the focused SLC image. There are many "autofocus" methods for estimation of the Doppler rate from the received data, such as map drift (MD) (Calloway and Donohoe, 1994), coherent MD (Samczynski and Kulpa, 2010), phase gradient autofocus (Wahl *et al.*, 1994), contrast optimization (Berizzi *et al.*, 2002), and shift-and-correlation (SAC) (Dall, 1991). The original SAC algorithm is proposed for the stripmap imaging mode, and improved by (Wu *et al.*, 2013) for estimating the Doppler rate of the spotlight SAR. However, algorithms are implicitly based on the assumption of the availability of well-isolated dominant scatterers and estimating the phase errors by selecting several range bins with little cross-terms effect. This cannot work effectively in most practical cases. A recently proposed autofocus method, is called "minimum entropy via subspace autofocus (MESA)," which has several advantages over the conventional methods (Cao *et al.*, 2010). These advantages are as follows: first the MESA is applicable to all range bins. The MESA does not need to select the range bins containing well-isolated dominant scatterers. Second, the MESA estimates the phase errors via a signal subspace so as to reduce the search dimensions greatly. Third, the MESA is robust, which can be ensured through the optimization method based on minimum entropy. The MESA method was employed to estimate Doppler rate at the reference range. The estimated Doppler rate of "070714" at the reference range is found to be '499.93 Hz·s^{-1}, against the initial Doppler rate, '559.55 Hz·s^{-1}, calculated by substituting the initial velocity of approximately 7592 m·s^{-1}, into Equation14.

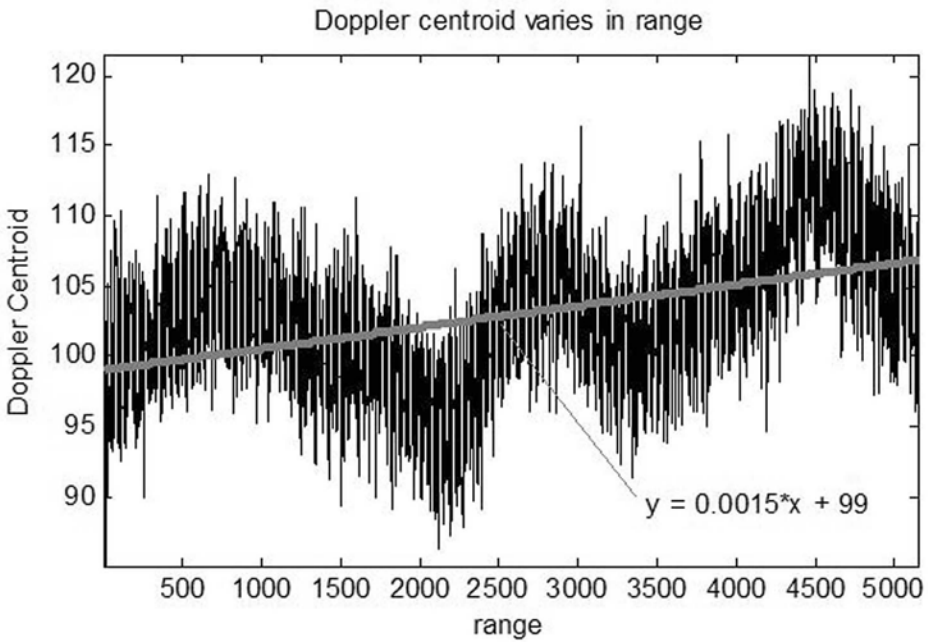

Figure 5. Doppler centroids estimated by the SDE algorithm, varying in the range of 85-120 Hz.

Estimation of the Forward Effective Velocities of the Sensor, the Near Range, and the Squint Angle

Following the identification of estimates representing Doppler centroids and Doppler rates, the form of Equation 15 suggests that either the forward effective velocities or the near range distance may be estimated. In this study, the near range distance is thought much more accurate than the velocity values, thus we concentrate solely on estimating the forward effective velocity.

Forward effective velocities at each point in time during data acquisition may be estimated in the following way. For the sake of gradually introducing the concept, here we will only describe the estimation of the forward effective velocities at the centre time of data acquisition. The method is described as follows.

First, the instantaneous Doppler centroids and Doppler rates at the center time are estimated. Doppler centroids and Doppler rates vary both in azimuth time and in range time; the variable cannot be neglected when the azimuth time is long. Thus, several azimuth lines around the center time need to be extracted and split in range direction to form several patches. In general, about one-tenth range lines of the synthetic aperture are enough for adequate velocity estimation. In this study, 1,024 range lines around the center time are extracted and split into 40 patches in range direction. Based on the 40 extracted range patches, the Doppler centroid and Doppler rate of each patch are estimated. These Doppler centroids and Doppler rates may then be considered Doppler centroids and Doppler rates of different range distances at the centre time. These Doppler centroids and Doppler rates vary with respect to range.

Second, the effective velocities are calculated using Equation 19. The estimated velocities for the first scene, "070714," are shown in Figure 6a, including correctly and incorrectly estimated velocities. The incorrectly estimated velocities are defined as those with values much smaller than the mean of all estimated velocities. The velocity is defined as the value below where the R_{ref} is the middle range distance of each patch:

$$v = \sqrt{\left(f_{dc}\lambda/2\right)^2 - \left(k_a R_{ref}\lambda/2\right)} \quad (19)$$

Third, the incorrectly estimated velocities are resampled using the mean value of the correctly estimated neighboring velocities.

Finally, the effective velocity for each range bin is obtained using polynomial curve fitting of correctly estimated and interpolated velocities. In this study, a straight line is used to fit the effective velocity for each range bin, as shown by the straight line in Figure 6a. The fitted effective velocities are referred to as "estimated effective velocities," with values varying from 7,271.7 m·s^{-1} in the near range to 7,094.6 m·s^{-1} in the far range.

As a comparison, effective velocities were also calculated from the GPS-determined orbits using GMTSAR (Sandwell *et al.*, 2011) software. These effective velocities are seen to vary from 7,174.9 m·s^{-1} in the near range to 7,167.6 m·s^{-1} in the far range, as evident in Figure 6b. Nakamura *et al.* (2007) shows that the GPS-determined orbits of ALOS-PALSAR are within −30 cm ±30 cm of the absolute evaluation determined by Satellite Laser Ranging (SLR) data. These GPS-determined effective velocities are referred to as "accurate effective velocities." After several experiments, we found the estimated effective velocity located in the middle range to be more accurate relative to the accurate velocity than comparison using velocities located in either the near or far range. The estimated velocity using the presented method at the middle range was 7,174.0 m·s^{-1}, with a difference of 2.7 m·s^{-1} from the GPS-determined velocity of 7,171.3 m·s^{-1} recorded at the same location; see Table 2. However, the differences between the velocities calculated using the GPS-determined orbit data and the presented method at the near range and far range are 96.8 m·s^{-1} and -73.0 m·s^{-1}, respectively, which clearly assume minimal data correlation. Therefore, as a result of the similarities expressed when using the middle range for both methods, we propose the use of the estimated velocity corresponding to this location, 7,174.0 m·s^{-1}, as a direct substitute for the GPS-determined effective velocities typically used for raw data focusing. However, to investigate the errors associated with the estimated velocities, at all range distances in this study the estimated velocities are artificially set to a default value of 7,177 m·s^{-1}, a marginally higher value than both the maximum GPS-determined effective velocity and the estimated velocity of the middle range found using the presented method, as shown in Figure 6b. As of now, all of the parameters needed for raw data focusing and generation of DEM and two pass differential phase maps are ready. However, we will continue to discuss the estimation of the other parameters that will not be used for raw data focusing and generation of DEM and two pass differential phase maps. Readers may reference it as needed.

For airborne SAR processing, the accurate near range distance may be more difficult to determine than the velocity. If the velocity is given, the near range distance can be estimated using Equation 21.

$$R_{ref} = \sqrt{\frac{2\left(f_{dc}\lambda/2\right)^2 - 2v^2}{\lambda k_a}} \qquad (21)$$

After sensor velocity estimation is established the squint angle can be calculated using Equation 22; the result associated with the data used in this study was recorded at 0.0970 degrees:

$$\beta = \arcsin\left(\frac{\lambda f_{dc}}{2v}\right) \qquad (22)$$

Estimation of the Forward Acceleration and Displacement Rate in LOS Direction

Short-period orbit errors associated with forward acceleration and displacement are typically less significant for spaceborne platforms than those associated with airborne studies. This is a result of their general orbiting locations well above the Earth's atmosphere. Regardless, the altitudes of spaceborne platforms do vary over time. The altitude may vary over the scale of a few hundred meters, while the forward velocity may vary on the scale of tens of meters in a scene of ALOS/PALSAR image.

The forward acceleration and displacement rate in LOS direction were estimated by using our previously proposed Xing method first introduced by Xing *et al.* (2009). For the

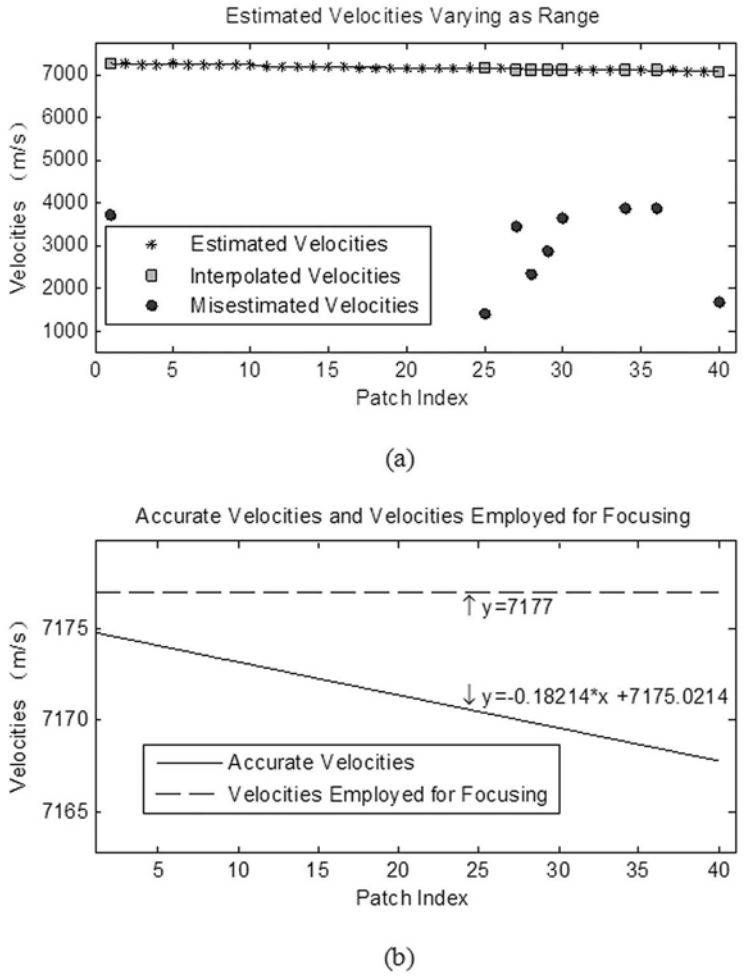

Figure 6. The estimated and accurate effective velocities: (a) estimated velocities by the proposed method; the properly estimated velocities are shown as "*", the incorrectly estimated velocities are shown as "o", and the resampled (interpolated) velocities are shown as "square", and (b) velocities employed for focusing (Dashed line) and accurate effective velocities calculated from GPS-determined orbits (Solid line).

Table 2. Velocities Estimated by the Proposed Method and Those Calculated from GPS-determined Orbits

Parameter name	Values estimated by Xing's method	Values from the GPS-determined orbits	Difference between the GPS-determined orbits and Xing's method
Forward effective velocity	7,174.0m·s^{-1}	7,171.3 m·s^{-1}	2.7m·s^{-1}
Forward acceleration	0.011 m·s^{-2}	0.005 m·s^{-2}	0.006 m·s^{-2}
Displacement rate	8.186 m·s^{-1}	5.543 m·s^{-1}	3.656 m·s^{-1}

Xing method the forward acceleration at the centre time of data acquisition was recorded as 0.011 $m \cdot s^{-2}$, while for the GPS determined orbits an acceleration of 0.005 $m \cdot s^{-2}$ was recorded. This represents a difference of 0.006 $m \cdot s^{-2}$ in forward acceleration. For displacement rate the Xing method produces a value of 8.186 $m \cdot s^{-1}$ with the GPS determined orbits producing a value of 5.543 $m \cdot s^{-1}$. This represents a displacement rate difference of 3.656 $m \cdot s^{-1}$. These data are shown in table 2.

The methods for estimation of forward acceleration and displacement rate without the use of GPS orbit data, as shown here, may prove very helpful for providing motion compensation data associated with airborne SAR systems. Due to the stability, SAR integration length, and image resolution, its relative use with spaceborne systems such as ALOS-PALSAR to implement motion compensation is less important than that of airborne SAR systems (Xing *et al.*, 2009; Cao *et al.*, 2010). As a consequence of this understanding, motion compensation based on forward acceleration and displacement rate were not included in the following experiments regarding the use of spaceborne data. The level of accuracy shown in the following experiments also suggests that it is not necessary to implement motion compensation for spaceborne systems.

Experiments

As part of the analysis, the pair of raw data scenes used in this study were focused using the estimated parameters obtained using the proposed methods (the processing steps are shown visually in the flow diagram of Figure 1). First, the order of real and imaginary parts of raw data was determined. The order of the real part and imaginary part was found to be normal for the scenes of concern with the real part stored before the imaginary part. Second, the sign of chirp rate in range was determined. The chirp rate was shown to be -5.18519×10^{11} $Hz \cdot s^{-1}$ with the pulses generated in the ALOS/PALSAR system acknowledged as "down-chirped" pulses. Third, the forward effective velocities and the squint angle of the LOS at the reference range were calculated using the Doppler centroids and Doppler rates, following from the Doppler centroid and Doppler rate determination. The estimated velocities at all range distances were then reset to 7,177 $m \cdot s^{-1}$, a little higher than the estimated velocity corresponding to the middle range of 7,174 $m \cdot s^{-1}$, as shown in Figure 6b. Finally, the same effective velocity, 7,177 $m \cdot s^{-1}$, was used to focus both scenes of raw data. The pair of SLC images focused using accurate GPS determined velocities and using the estimated velocities determined from the raw data are shown in Figure 7 a and 7b, respectively.

On visual inspection, it is difficult to distinguish between the pair of SLCs in Figure 7a from those of Figure 7b. In order to investigate more closely we compared the coherence maps (shown in Figure 8), DEMs (shown in Figure 9), and differential unwrapped phase maps (shown in Figure 10). These extra data sets were created from the interferometric analysis of these two pairs of SLC images.

Note that a high-precision baseline is very important for the generation of our DEMs and differential unwrapped phase maps in the absence of accurate orbit data. We refined the baseline using the revised ROI_PAC (Buckley, 2002; Rosen, 2004) after the ALOS default baseline value of 500 m was given. In the following analysis, the absolute difference is defined as the difference between the measured value and the actual value. Relative difference is defined as the ratio of the absolute error of the measurement to the accepted measurement.

Discussion

Figure 8e shows that approximately 95 percent of the coherence values in both coherence maps possess values of over 0.1, with ~30 percent showing values above 0.5. This data distribution indicates a good level of coherence between SLC

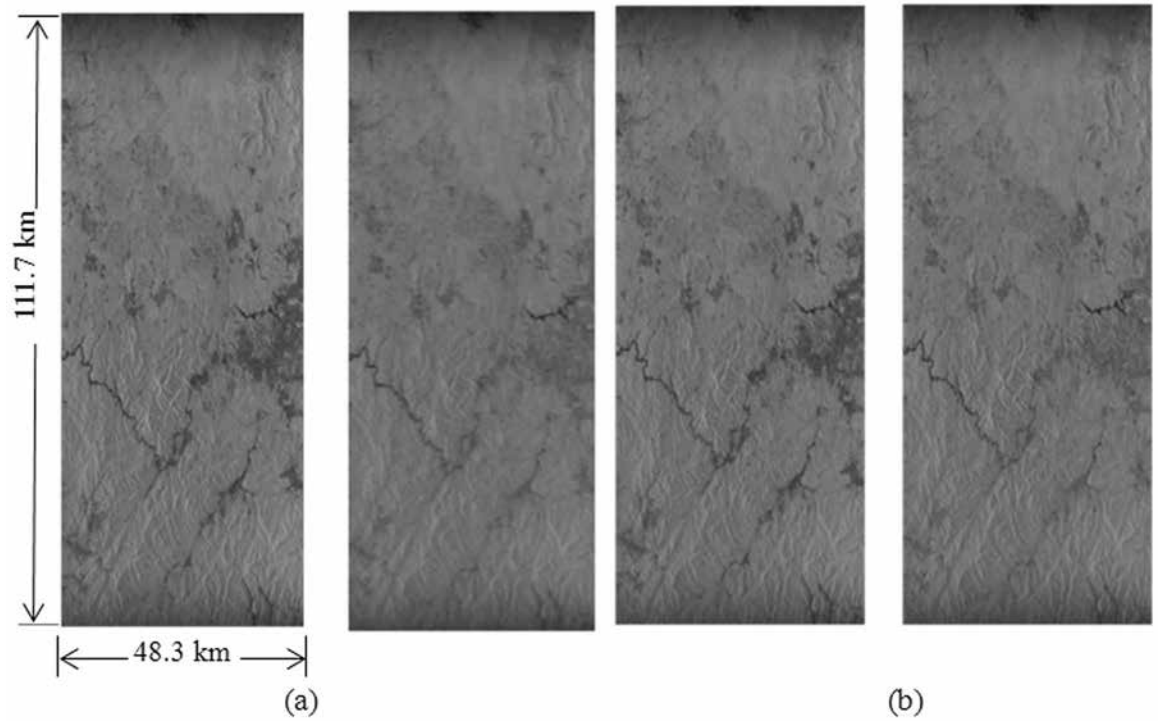

Figure 7. SLC images focused from a pair of raw data: (a) presents the magnitude of the pair of SLC images focused using accurate velocities, and (b) presents the magnitude of the pair of SLC images focused using estimated velocities.

pairs focused using both the accurate and estimated velocities. The similarity in trends seen visually and statistically in Figure 8 is representative of the effectiveness of the use of estimated velocities within the focusing process. Figure 8 f also shows that ~93 percent of the coherence difference values are within ±0.06. At the higher relative difference values bound of ±0.1 this percentage increases to 98.7 percent. Figure 8g shows that ~91.4 percent of the relative difference values are within ±0.2, representing 20 percent difference. At the higher relative difference values bound of ±1, i.e., 100 percent difference, this percentage increases to 99.8 percent. The visual and statistical similarities highlight how the two independent focusing methods produce extremely similar coherence maps.

Figure 9e shows that ~92 percent of the absolute heights of each pixel published in the DEM that have been created from the pair of SLC images focused using the estimated velocities are within ±1 m of the absolute heights determined using the accurate velocity method. At the higher error bound of ±5 m this percentage increases to 99.9 percent. Further analysis of this data Figure 9f suggests that approximately 93 percent of the DEM values are located within 2 percent of the accurate velocity DEM derivations. At the higher relative difference values bound of ±10 percent this percentage increases to 99.9 percent. The low DEM relative difference values are another clear indicator of the effectiveness of the focusing method presented in the absence of accurate GPS derived velocities.

Figure 10e shows that about 95 percent of the differential unwrapped phase values of each pixel created from the pair of SLC images after being focused using estimated velocities are within ±0.002 radians of the accurate velocity equivalent. This implies that 95 percent of phases have an error of less than 0.04 mm displacement change in LOS direction. At the difference values bound of ±0.1 radians these bounds encompass 99.8 percent of differential unwrapped pixel phases. This low phase error will not affect ALOS interferometry that has the capability to measure centimeter-scale changes in deformation (Sandwell, 2008). Besides, Figure 10f shows that about 93 percent of the relative difference values are within ±0.2. At the higher relative difference values bound of ±1 this percentage increases to 99.1 percent. If we now compare Figure 10a and 10d, we can deduct that the areas with high relative difference are along zero deformation, and are not concerns of interferometry. As a consequence, the presented focusing method in the absence of accurate GPS-derived velocities may serve as an alternative method for deformation monitoring although many relative difference values appear slightly high.

Conclusions

In this study, a novel method for determining the order of real and imaginary parts of raw data, and the sign of chirp rate are proposed. The forward effective velocities of the sensor, near range distance, squint angle of LOS, forward acceleration of the sensor and sensor displacement rate in LOS direction in

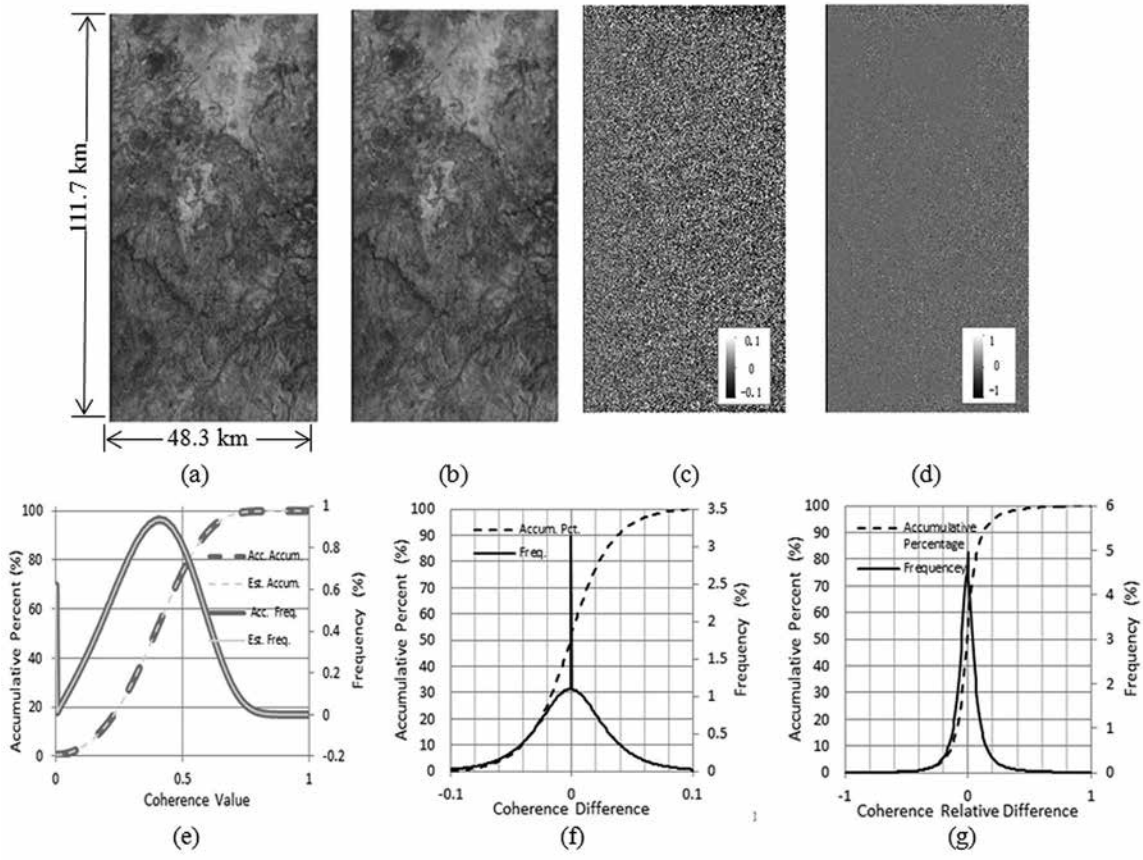

Figure 8. Coherence maps of the two pairs of SLC images: (a) and (b) are the coherence maps of the two pairs of SLC images focused using accurate GPS-determined velocities and using estimated velocities, respectively; (c) is a difference map between coherence maps created from accurate GPS-derived velocities and estimated velocities; (d) is a relative difference map between coherence maps created from accurate velocities and estimated velocities; (e) is accumulative percentage and frequency distribution chart; (f) is accumulative percentage and frequency distribution chart of coherence difference map; and (g) is accumulative percentage and frequency distribution chart of coherence relative difference map.

the absence of accurate orbit data are then extracted. The accuracy of these estimated parameters is compared with those produced using accurate orbit data associated with SAR scenes acquired by ALOS-PALSAR L-Band SAR. The comparison, based on multi-levels, includes analysis of SLCs, coherence maps, DEMs, and dual-pass differential unwrapped phase maps. The comparative analysis shows that the correlation coefficient between the coherence maps created using accurate parameters and estimated parameters is 0.99, indicating that when using interferometric methods the two raw data focusing methods are almost inseparable. This has positive connotations for DEM generation and forest height estimation among other practical and environmental applications where metadata, as accurate as that provided for ALOS-PALSAR, is not available. For the DEMs, about 92 percent of the absolute height differences of each pixel between the two DEMs formed using different raw data focusing techniques are within ±1m with 99.9 percent contained within the limit of ±5m. For the absolute phase values approximately 95 percent of the absolute phase differences of each pixel between the unwrapped phase maps associated with the two focusing methods are within ±0.002 radians rising to 99.8 percent within the limits of ±0.1 radians.

This level of accuracy suggests that it is acceptable to use the novel methods proposed in this study to create SLCs, DEMs and dual-pass differential phase maps. Producing parameters using the methods of this study will provide a helpful reference for the estimation of parameters associated with airborne SAR systems which do not possess high-accuracy INS and GPS.

Acknowledgments

The authors would like to acknowledge financial support from the National Key Technology R&D Program (2013BAC03B02; 2012BAC19B04; 2012BAJ15B04), the Research Fund for the Doctoral Program of Higher Education of China (20130141130003), the open foundation of Key Laboratory of Precise Engineering & Industry Surveying of National Administration of Surveying, Mapping & Geoinformaton (PF2013-14), and the International Science and Technology Cooperation Project of China (2012DFA31290). The SAR raw data used in this study were provided by Guoqing Sun. The authors would like to thank many of our colleagues, and in particular Wenli Huang, and Wenjian Ni, for their valuable comments.

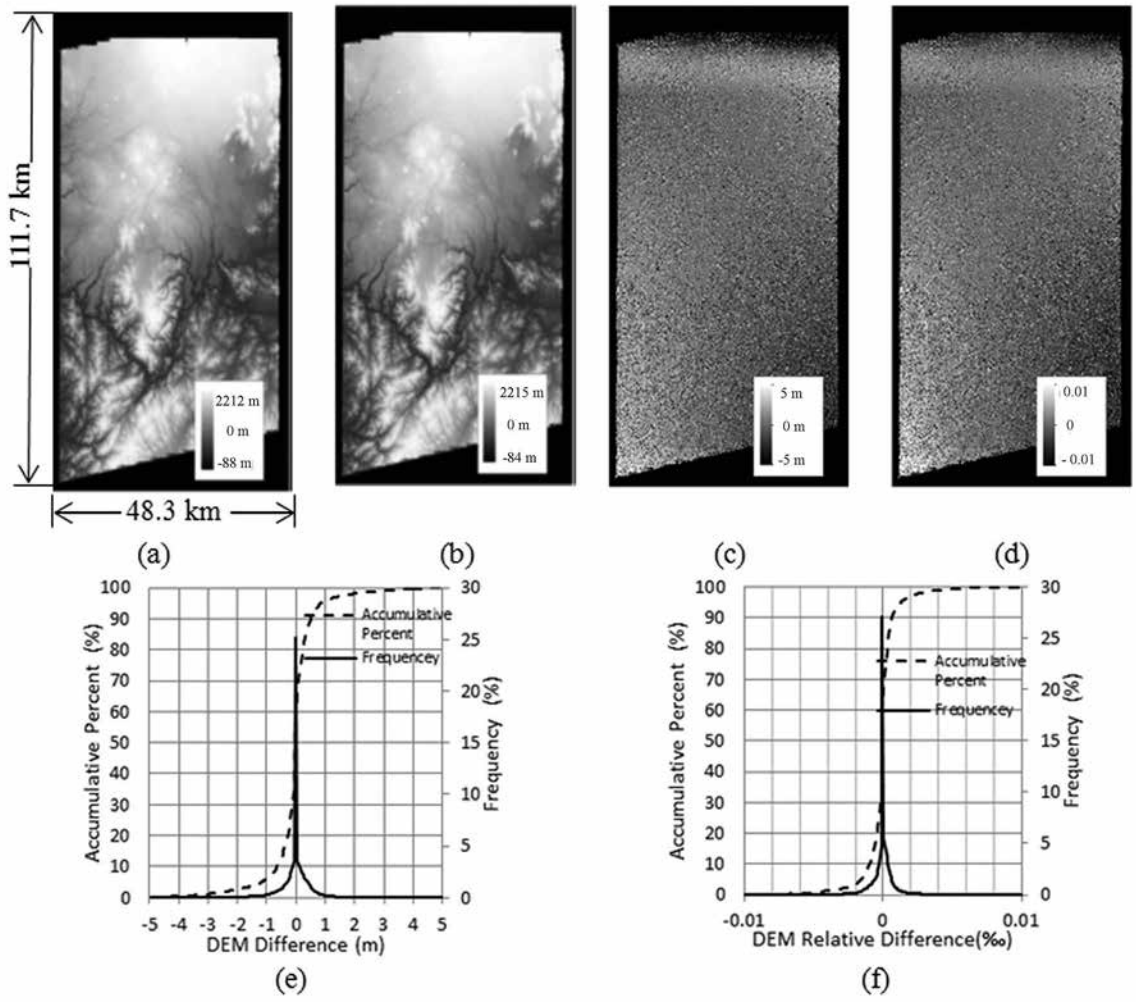

Figure 9. DEMs created from the two pairs of SLC images focused using accurate GPS-derived velocities and estimated velocities. Image sizes are 5,270 pixels (in range) × 8,312 pixels (in azimuth). (a) and (b) are DEMs created from two pairs of SLC images focused using accurate GPS derived velocities and estimated velocities, respectively; (c) is a difference map between DEMs created from accurate velocities and estimated GPS-derived velocities; (d) is a relative difference map between DEMs created from accurate velocities and estimated GPS derived velocities; (e) is accumulative percentage and frequency distribution chart of DEM difference map; and (f) is accumulative percentage and frequency distribution chart of DEM relative difference map.

References

Bamler, R., 1991. Doppler frequency estimation and the Cramer-Rao bound, *IEEE Transactions on Geoscience and Remote Sensing*, 29(3):385–390.

Bamler, R., and H. Runge, 1991. PRF-ambiguity resolving by wavelength diversity, *IEEE Transactions on Geoscience and Remote Sensing*, 29(6):997–1003.

Berizzi, F., E. Dalle Mese, and M. Martorella, 2002. Performance analysis of a contrast-based ISAR autofocusing algorithm, *Proceedings of the IEEE Radar Conference*, IEEE, pp. 200–205.

Buckley, S.M., 2000. *Radar Interferometry Measurement of Land Subsidence*, The University of Texas at Austin, Austin, Texas.

Calloway, T.M., and G.W. Donohoe, 1994. Subaperture autofocus for synthetic aperture radar, *IEEE Transactions on Aerospace and Electronic Systems*, 30(2): 617–621.

Cao, P., M. Xing, G. Sun, Y. Li, and Z. Bao, 2010. Minimum entropy via subspace for ISAR autofocus, *IEEE Geoscience and Remote Sensing Letters*, 7(1):205–209.

Crosetto, M., 2002. Calibration and validation of SAR interferometry for DEM generation, *ISPRS Journal of Photogrammetry and Remote Sensing*, 57(3):213–227.

Cumming, I.G., P.F. Kavanagh, and M.R. Ito, 1986. Resolving the Doppler ambiguity for spaceborne synthetic aperture radar, *Proceedings of IGARSS'86: Remote Sensing: Today's Solutions for Tomorrow's Information Needs*, pp. 1639–1643.

Cumming, I.G., and S. Li, 2007. Adding sensitivity to the MLBF Doppler centroid estimator, *IEEE Transactions on Geoscience and Remote Sensing*, 45(2):279–292.

Dan, J., 1991. A new frequency domain autofocus, *Proceedings of the Geoscience and Remote Sensing Symposium, 1991*. IGARSS '91, Remote Sensing: Global Monitoring for Earth Management., International, Espoo, Finland, pp. 1069–1072.

Dell'Acqua, F., and D.A. Polli, 2011. Post-event only VHR radar satellite data for automated damage assessment: A Study on COSMO/SkyMed and the 2010 Haiti earthquake, *Photogrammetric Engineering & Remote Sensing*, 77(10):1037–1043.

Gernhardt, S., and R. Bamler, 2012. Deformation monitoring of single buildings using meter-resolution SAR data in PSI, *ISPRS Journal of Photogrammetry and Remote Sensing*, 73(SI):68–79.

Herrera, G., R. Tomás, J.M. Lopez-Sanchez, J. Delgado, F. Vicente, J. Mulas, G. Cooksley, M. Sanchez, J. Duro, A. Arnaud, P. Blanco, S. Duque, J.J. Mallorqui, R. De la Vega-Panizo, and O. Monserrat, 2009. Validation and comparison of advanced differential

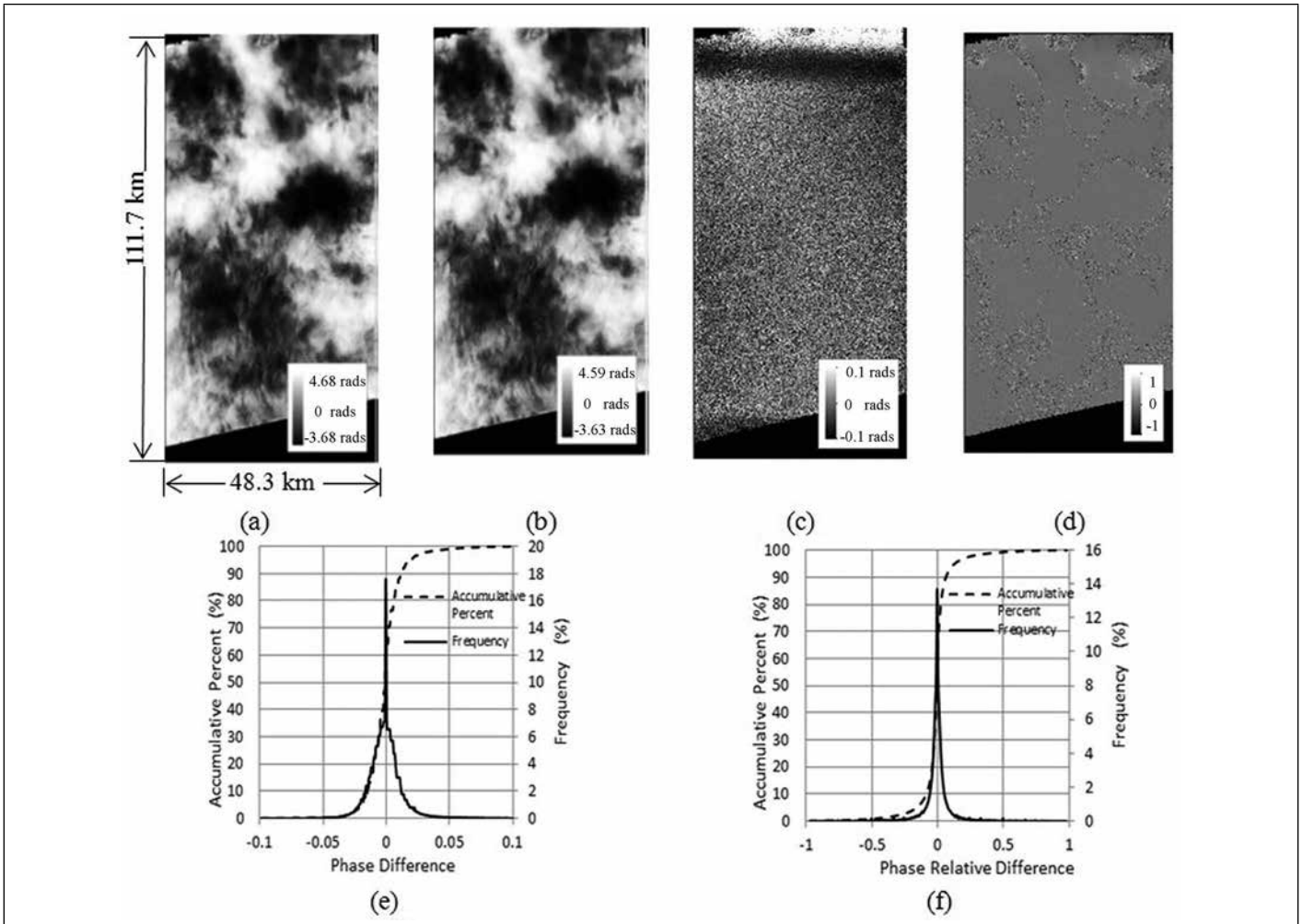

Figure 10. Dual-pass differential unwrapped phase maps created from two pairs of SLC images focused using accurate GPS-derived velocities and estimated velocities using the methods presented in this study. Image size is 1,287 pixels (in range) × 1,921 pixels (in azimuth). (a) and (b) are the differential phase maps created from the two pairs of SLC images focused using accurate GPS-derived velocities and estimated velocities, respectively; (c) is a difference map between differential phase map created from accurate velocities and the differential phase map created from estimated velocities; (d) is a relative difference map between differential phase map created from accurate velocities and the differential phase map created from estimated velocities; (e) is accumulative percentage and frequency distribution chart of the difference map; and (f) is accumulative percentage and frequency distribution chart of phase relative difference map.

interferometry techniques: Murcia metropolitan area case study, *ISPRS Journal of Photogrammetry and Remote Sensing*, 64(5):501–512.

Jin, M.Y., 1986. Optimal Doppler centroid estimation for SAR data from a quasi-homogeneous source, *IEEE Transactions on Geoscience and Remote Sensing*, GE-24(6):1022–1025.

Jones, C.E., and B.A. Davis, 2011. High resolution radar for response and recovery monitoring containment booms in Barataria Bay, *Photogrammetric Engineering & Remote Sensing*, 77(2):102–105.

Kaya, G.T., N. Musaoglu, and O.K. Ersoy, 2011. Damage assessment of 2010 Haiti earthquake with post-earthquake satellite image by support vector selection and adaptation, *Photogrammetric Engineering & Remote Sensing*, 77(10):1025–1035.

Gerke, M., and N. Kerle, 2011. Automatic structural seismic damage assessment with airborne oblique Pictometry imagery, *Photogrammetric Engineering & Remote Sensing*, 77(9):885–898.

Kong, Y.K., B.L. Cho, and Y.S. Kim, 2005. Ambiguity-free Doppler centroid estimation technique for airborne SAR using the Radon transform, *IEEE Transactions on Geoscience and Remote Sensing*, 43(4):715–721.

Madsen, S.N., 1989. Estimating the Doppler Centroid of SAR data, *IEEE Transactions on Aerospace and Electronic Systems*, 25(2):134–140.

Martone, M., B. Bräutigam, P. Rizzoli, C. Gonzalez, M. Bachmann, and G. Krieger, 2012. Coherence evaluation of TanDEM-X interferometric data, *ISPRS Journal of Photogrammetry and Remote Sensing*, 73(SI):21–29.

Nakamura, R., S. Nakamura, N. Kudo, and S. Katagiri, 2007. Precise orbit determination for ALOS, *Proceedings of the 20th International symposium on space flight dynamics*, Annapolis, Maryland, pp. 24–28.

Rosen, P.A., S. Hensley, G. Peltzer, and M. Simons, 2004. Updated repeat orbit interferometry package released, *Eos, Transactions American Geophysical Union*, 85(5):47–47.

Rossi, C., F. Rodriguez Gonzalez, T. Fritz, N. Yague-Martinez, and M. Eineder, 2012. TanDEM-X calibrated Raw DEM generation, *ISPRS Journal of Photogrammetry and Remote Sensing*, 73(SI):12–20.

Samczynski, P., and K.S. Kulpa, 2010. Coherent mapdrift technique, *IEEE Transactions on Geoscience and Remote Sensing*, 48(3):1505–1517.

Sandwell, D., R. Mellors, X. Tong, M. Wei, and P.Wessel, 2011. Open radar interferometry software for mapping surface deformation, *Eos, Transactions*, American Geophysical Union, 92(28):234–234.

Sandwell, D.T., D. Myer, R. Mellors, M. Shimada, B. Brooks, and J. Foster, 2008. Accuracy and resolution of ALOS interferometry: Vector deformation maps of the Father's Day intrusion at Kilauea, *Transactions on Geoscience and Remote Sensing*, IEEE, 46(11):3524–3534.

Wahl, D., P. Eichel, D. Ghiglia, C. Jakowatz Jr., 1994. Phase gradient autofocus - A robust tool for high resolution SAR phase correction, *IEEE Transactions on Aerospace and Electronic Systems*, 30(3):827–835.

Wong, F., and I.G. Cumming, 1996. A combined SAR Doppler centroid estimation scheme based upon signal phase, *IEEE Transactions on Geoscience and Remote Sensing*, 34(3):696–707.

Wu, Y., G. Sun, X. Xia, M. Xing, and Z. Bao, 2013. An improved SAC algorithm based on the Range-Keystone Transform for Doppler rate estimation, *Geoscience and Remote Sensing Letters*, IEEE, 10(4):741–745.

Xing, M.D., X.W. Jiang, R.B. Wu, F. Zhou, and Z. Bao, 2009. Motion compensation for UAV SAR based on raw radar data, *IEEE Transactions on Geoscience and Remote Sensing*, 47(8):2870–2883.

Yu, W., and Z. Zhu, 1997. Comparison of Doppler centroid estimation methods in SAR, *Proceedings of the IEEE 1997 National Aerospace and Electronics Conference*, NAECON 1997, Dayton, Ohio, pp. 1015–1018.

Zhang, J.X., Z. Zhao, G.M. Huang, Z. Lu, 2012. CASMSAR: An integrated airborne SAR mapping system, *Photogrammetric Engineering & Remote Sensing*, 78(11):1110–1114.

Zhang S.X., M.D. Xing, X.G. Xia, L. Zhang, R. Guo, and Z. Bao, 2013. Focus improvement of high-squint SAR based on azimuth dependence of quadratic range cell migration correction, *Geoscience and Remote Sensing Letters*, IEEE, 10(1):150–154.

(Received 18 September 2013; accepted 23 December 2013; final version 03 April 2014)